Investigating the conformal behavior of SU(2) with one adjoint Dirac flavor

Andreas Athenodorou [1,*] Ed Bennett [2,†] Georg Bergner [3,‡] and Biagio Lucini [4,§]

[1]*Dipartimento di Fisica, Università di Pisa and INFN,*
Sezione di Pisa, Largo Pontecorvo 3, 56127 Pisa, Italy
[2]*Swansea Academy of Advanced Computing, Swansea University,*
Fabian Way, Swansea SA1 8EN, United Kingdom
[3]*University of Jena, Institute for Theoretical Physics, Max-Wien-Platz 1, D-07743 Jena, Germany*
[4]*Department of Mathematics, Swansea University, Fabian Way, Swansea SA1 8EN, United Kingdom*

We present a major update on our investigations of SU(2) gauge theory with one Dirac flavor in the adjoint representation on the lattice. In particular, we consider larger volumes as well as four different values of the gauge coupling. We provide results for the spectrum including gluonic, fermionic, and hybrid observables; Polyakov loops; and the anomalous dimension of the fermionic condensate from the Dirac mode number. These data confirm that the theory is close to the lower boundary of the conformal window for adjoint fermions. Our investigations provide important insights regarding the realization of different infrared scenarios that have been conjectured for this theory.

I. INTRODUCTION

The SU(2) gauge theory with N_f Dirac fermions in the adjoint representation has seen many interesting recent applications in theoretical studies ranging from composite Higgs models to topological phases related to systems of condensed matter physics. The most prominent examples of these theories are the $N_f = 2$ case, called Minimal Walking Technicolor, and supersymmetric Yang-Mills theory, corresponding to the case with one Majorana fermion. Recently, also the case of the $N_f = 1$ Dirac fermion gained much interest. It has been considered in the context of semi-classical analysis [1] and volume independence, leading to the conjecture of emergent fermion symmetry event in the nonsupersymmetric case [2]. Another line of interest has been the relation of chiral symmetry breaking and confinement. The most recent interest has come from the consideration of 't Hooft anomaly matching and topological phase transitions [3,4]. Although all of these investigations reveal interesting aspects and conjectures about the nonperturbative regime, it is still unclear what kind of phase is realized at low

temperatures. It should be stressed that all conjectures and studies depend on this basic knowledge of the theory.

The main motivation of our previous investigations of the SU(2) gauge theory with one adjoint Dirac fermion has been the question about signatures of a conformal window related to composite Higgs scenarios. In these scenarios, the Higgs sector emerges as a low-energy manifestation of novel strong dynamics [5–9]. This new strong interaction is able to explain the observed electroweak symmetry breaking phenomenology if the following three conditions are met:

(1) The theory is near the onset of the conformal window.
(2) The anomalous dimension of the chiral condensate is of order 1.
(3) A parametrically light scalar (the would-be Higgs boson) is in the spectrum. The first two conditions [10,11] are needed for compatibility with electroweak precision data [12], while the third condition is determined by the direct observation of the Higgs boson and no other previously unknown nearby state. Numerical lattice simulations have provided important information about the realization of these conditions in different theories. Interesting candidates are in particular gauge theories coupled to fermions in higher representations since these require a smaller number of fermion fields to reach the conformal window [13–16]. One example of a gauge theory which, according to numerical data, is inside the conformal window is SU(2) gauge theory with two

---

*andreas.athinodorou@pi.infn.it
†e.j.bennett@swansea.ac.uk
‡georg.bergner@uni-jena.de
§b.lucini@swansea.ac.uk

adjoint Dirac flavors [17–29]. However, the low mass anomalous dimension,[1] $\gamma_\star = 0.38(2)$ [31], at the infrared fixed point disfavors this model for phenomenological applications. Meanwhile, also a first study with three Majorana fermions in the adjoint representation has appeared [32], showing an increasing mass anomalous dimension toward a lower fermion content of the theory.

The identification of a theory with an at least nearconformal behavior and a large mass anomalous dimension has been the main motivation for our previous studies of SU(2) with a single adjoint Dirac flavor. In fact, given that the theory with two adjoint flavors was observed to be well within the conformal window, there is the possibility that the theory with a single adjoint flavor sits at the onset of conformality. Such behavior is required for phenomenologically viable theories to explain electroweak symmetry breaking at a fundamental level. In this context, a first obvious but very relevant question is whether the theory is just outside or inside the conformal window. The theory can later be extended by additional fundamental fermions to provide a viable extension of the Standard Model [33,34].

Close to the onset of the conformal window, it is hard to distinguish a conformal from a chiral symmetry breaking scenario.[2] In such a (near-)conformal regime, large scaling corrections are also expected. Therefore, a very detailed study of the dependence on simulation parameters is required. In this respect, our first investigations [36] utilizing only a single lattice spacing have provided only limited insight. A later study in Ref. [37] considered mainly the same parameter range for a different analysis. For this reason, we provide here a substantial extension of our previous simulations considering a range of different gauge couplings and a large number of additional ensembles in order to improve on our first investigations of the theory.

Another line of motivation for an investigation of SU(2) with one adjoint Dirac flavor is a general scan in the parameter space of strongly interacting theories to identify common patterns and relate them to analytical predictions, for example based on gauge/gravity duality. In this context, we have investigated the ratio of lightest spin-2 and spin-0 resonances [38]. We have shown that possible nontrivial universal characteristic in the landscape of strongly interacting gauge theories can be identified. These could later on help searches for candidate theories describing realistic Standard Model extensions.

An interesting further relation of the theory is with $\mathcal{N} = 2$ super-Yang-Mills with gauge group SU(2), in the limit of a large scalar mass which leads to complete supersymmetry breaking. In $\mathcal{N} = 2$ super-Yang-Mills, confinement is

known to arise through the dual superconductor mechanism resulting from magnetic monopole condensation [39]. The breaking of supersymmetry by a finite scalar mass has been considered in Ref. [40], in which the authors argue that in the large mass limit chiral symmetry breaking is at play.

Our investigations are based on the first-principles method of numerical Monte Carlo simulations on a spacetime lattice. In Sec. II, we provide a summary of the continuum properties, and lattice action, of the theory. We also explain the main observables and parameters considered in this study. Additional information about the simulation setup and the lattice formulation can be found in our previous publication [36].

The main results presented in Sec. III start with a discussion on the general limitations of the parameter range due to phase transitions and topological freezing. We show that our simulations are not limited by these general systematic effects. The obtained bound state particle spectrum at different fermion masses is presented in Sec. III C. The main result of this paper regarding mass anomalous dimension are presented in Sec. III D. Assuming conformal scaling, we determine the mass anomalous dimension from the particle spectrum and mode number. The results confirm a significantly larger anomalous dimension than in the two Dirac flavor case. However, they also reveal relevant scaling corrections. We discuss as an alternative scenario also a fit according to chiral perturbation theory in Sec. III E. As a short update regarding our work in Ref. [38], we also discuss the ratio between the spin-2 and spin-0 glueballs. At the end of the paper, we discuss the implications for infrared scenarios of the theory in Sec. IV.

II. SUMMARY OF THE THEORY AND CONSIDERED OBSERVABLES

We investigate the SU(2) gauge theory with a single Dirac fermion in the adjoint representation (SU2Nf1Adj). Although our goal is to understand the theory in the massless limit, numerical simulations require a finite fermion mass. We, therefore, simulate at different fermion masses and investigate how the massless limit is approached. Our primary goal is to understand whether chiral symmetry is spontaneously broken in the massless limit or the theory is IR conformal. In case of spontaneous chiral symmetry breaking, chiral perturbation theory would be sufficient to describe the low-energy effective theory at small fermion masses. On the contrary, if our theory is IR conformal, the data will be in accordance with the scaling predictions of a mass-deformed IR conformal gauge theory. It is possible that SU2Nf1Adj is in the QCD-like phase with confinement and chiral symmetry breaking but close to the onset of the conformal window. If such a scenario holds, the system might demonstrate mass-deformed conformal behavior within an intermediate-energy regime between the chiral symmetry breaking scale Λ_{IR} and the perturbative scale in ultraviolet Λ_{UV}, while for energies below Λ_{IR}, the system will be

---

[1]The actual mass anomalous dimension might even be lower; see Ref. [30] and references therein.

[2]We observe that for fermions in the adjoint representation the chiral symmetry breaking scale can be separated from the confinement scale; see Ref. [35] for a recent discussion.

correctly described by chiral perturbation theory. The latter possibility refers to the so-called near-conformal or walking scenario. We focus mainly on the distinction of chiral symmetry breaking and IR conformal scenario, but we also discuss other possible IR scenarios in the final conclusions.

The Lagrangian of SU2Nf1Adj in Minkowski space is defined as

$$\mathcal{L} = \bar{\psi}(x)(i\slashed{D} - m)\psi(x) - \frac{1}{2}\text{Tr}(G_{\mu\nu}(x)G^{\mu\nu}(x)), \quad (1)$$

with $\slashed{D} = (\partial_\mu + igA_\mu(x))\gamma^\mu$, γ_μ being the Dirac matrices, $A_\mu(x) = \sum_a T^a A_\mu^a(x)$ with $a = 1, 2, 3$, and the T_a being the Lie algebra generators of SU(2) in the adjoint representation. The field strength tensor is defined as $G_{\mu\nu} = \partial_\mu A_\nu(x) - \partial_\nu A_\mu(x) + ig[A_\mu(x), A_\nu(x)]$, with g being the gauge coupling of the theory, and the trace is taken over the gauge group. Notation and conventions are explained in Ref. [36].

The adjoint representation is real and, as a consequence, does not mix real and imaginary parts of the Dirac spinor. This enables us to decompose the Dirac spinor in Majorana components as follows,

$$\xi_+ = \frac{\psi + C\bar{\psi}^{\mathrm{T}}}{\sqrt{2}}, \qquad \xi_- = \frac{\psi - C\bar{\psi}^{\mathrm{T}}}{\sqrt{2}i}, \qquad (2)$$

such that

$$\psi = \frac{1}{\sqrt{2}}(\xi_+ + i\xi_-). \qquad (3)$$

In the above expressions, C is the charge conjugation matrix; both ξ_+ and ξ_- are invariant under charge conjugation symmetry by construction. Equation (1) can, thus, be reformulated as

$$\mathcal{L} = \frac{1}{2}\sum_k \bar{\xi}_k(x)(i\slashed{D} - m)\xi_k(x) - \frac{1}{2}\text{Tr}(G_{\mu\nu}(x)G^{\mu\nu}(x)), \quad (4)$$

where $k = +, -$. This flavor structure (in terms of the Majorana components) gives rise to a nontrivial chiral symmetry breaking pattern.

The general chiral symmetry breaking pattern that can be identified from this formulation is

$$\text{SU}(2N_{\mathrm{f}}) \mapsto \text{SO}(2N_{\mathrm{f}}). \qquad (5)$$

In the present case of $N_{\mathrm{f}} = 1$, there are hence two Goldstone bosons in this model if chiral symmetry is spontaneously broken. The unbroken SO(2) is equivalent to U(1) baryon number in Dirac fermion formulation.

The identification of quantum numbers for two-fermion operators has been presented in our earlier paper [36]. These are in principle generalization of the meson operators in

QCD, but the labeling is done according the unbroken U(1). Hence, there are mesons transforming trivially under this symmetry and baryons (or diquark) operators that carry baryon number ± 2. The operators for the Goldstone bosons correspond to scalar baryons for which the fermion contractions are similar to the pions in QCD. In these extended measurements, we do not consider operators with disconnected contributions. Besides the scalar baryons ($\psi^T C\gamma_5\psi$), we consider also the pseudoscalar baryon ($\psi^T C\psi$), the vector baryon ($\psi^T C\gamma_k\gamma_5\psi$), and the vector meson ($\bar{\psi}\gamma_k\psi$).

A. Lattice action and observables

Our simulations are based on a lattice action consisting of a Wilson gauge and fermion action given by

$$S = S_{\mathrm{G}} + S_{\mathrm{F}}, \qquad (6)$$

where

$$S_{\mathrm{G}} = \beta\sum_p \text{Tr}\left[1 - \frac{1}{2}U(p)\right] \qquad (7)$$

and

$$S_{\mathrm{F}} = \sum_{x,y}\bar{\psi}(x)D(x, y)\psi(y). \qquad (8)$$

Here, $U(p)$ is the lattice plaquette, and S_{G} and S_{F} are, respectively, the pure gauge part and the fermionic contribution in the action. The massive Dirac operator is defined as

$$D(x, y) = \delta_{x,y} - \kappa[(1 - \gamma_\mu)U_\mu(x)\delta_{y,x+\mu} \\ + (1 + \gamma_\mu)U_\mu^\dagger(x - \mu)\delta_{y,x-\mu}], \qquad (9)$$

where $U(p)$ is the lattice plaquette, $\kappa = 1/(8 + 2am)$ is the hopping parameter, a is the lattice spacing, and m is the bare fermion mass. Further details of the lattice representation and algorithms can be found in our earlier work [36]. As detailed in this reference, particle masses are obtained from correlators of operators projecting onto the selected quantum numbers. Note that the Wilson fermions break chiral symmetry and require the inclusion of an additive and multiplicative renormalizaton of the fermion mass. The *partially conserved axial current* (PCAC) defines a mass m_{PCAC} which requires only multiplicative renormalization, which is used as a proxy of the renormalized fermion mass. The lattice technology used to define correlators and the m_{PCAC} mass and to compute them on the lattice is by now standard (see, e.g., Ref. [41] for a more extended treatment).

For the mesonic observables and the generation of the configurations, we have used HIREP[3] [17,27]. The results

---

[3]See https://github.com/claudiopica/HiRep for the HiRep source code.

were also cross-checked with a code developed for simulations of super-Yang-Mills theories [42]. The latter code has also been used to measure a spin-$\frac{1}{2}$ hybrid fermion state which is constructed in the continuum from the operator

$$O_{\text{spin}-\frac{1}{2}} = \sum_{\mu,\nu} \sigma_{\mu\nu} \text{tr}[F^{\mu\nu}\xi], \qquad (10)$$

where $\sigma_{\mu\nu} = \frac{1}{2}[\gamma_\mu, \gamma_\nu]$. This state, which can be seen as a bound state of a fermion and a gluon, was computed using the tools described in Ref. [42]. Gluonic observables (and in particular glueball and torelon states) have been studied using the techniques exposed in Ref. [43]. Further details are explained in sections presenting the numerical results, and raw data are available in Ref. [44].

In addition, we also determine the scale setting quantities t_0 and w_0 from the gradient flow. These are introduced in Sec. III B. We also consider the string tension with the methods already explained in Ref. [36].

The theory requires a careful consideration of the simulation parameter range. A detailed investigation over the parameter space in Ref. [36] shows a strong signal for a bulk phase transition at around $\beta \approx 1.9$, $am \approx -1.65$. The requirement to connect with continuum limit, therefore, imposes to simulate at $\beta > 1.95$. In order to avoid the bulk phase and retrieve the desired continuum physics, in our previous study, we have chosen the value $\beta = 2.05$. According to this analysis, this value of the gauge coupling is in the region connected to continuum physics. However, it is still quite close to the bulk phase and, assuming a positive β-function, corresponds to a rather coarse lattice. The choice was dictated by the necessity to study large volumes in order to explore the infrared behavior of the theory while keeping under control the computational cost. However, a thorough assessment of discretization effects requires studies over a range of increasing βs, in order to extrapolate to the continuum limit. For these simulations, a higher computational effort is needed. Another reason to simulate at weaker couplings is related to the generic continuum structure of an IR conformal gauge theory, which, in addition to the asymptotically free phase connected with the ultraviolet Gaussian fixed point, is expected to have a strong coupling phase in which the coupling decreases at large distances [45]. Therefore, if the lattice model is investigated at strong coupling, there is the potential danger that in the continuum it will describe the latter phase of the model, which is not the one we are interested in.

Simulations of a range of larger gauge couplings require a consideration of additional relevant effects that can affect the results. Due to the decreased lattice spacing, the physical lattice volume could become small enough to induce a transition to a phase with broken center symmetry in some direction indicated by a nonzero expectation value of spatial or temporal Polyakov loops. Another important

effect is topological freezing. At larger values of β, the topological charge fluctuations are strongly suppressed, and hence the simulation becomes nonergodic. We have performed a detailed consideration of these effects in Secs. III A and III B.

Our investigation spans over four values of β, namely, $\beta = 2.05$, 2.10, 2.15, and 2.20, as well as over a broad range of bare masses am. The details of all the ensembles produced for the purposes of this work are presented in the Appendix A, and are available in machine-readable form in Ref. [44]. For simplicity, we denote our ensembles as DBiMj, where the first index $i = 1, \ldots, 4$ refers to the four values of β, while the second index $j = 1, \ldots$ refers to the choice of mass. Furthermore, we use asterisks as subscripts on this notation to denote smaller volumes produced for investigating finite-volume effects and possible phase transitions.

III. RESULTS

A. Expectation value of Polyakov loops—Center symmetry

The introduction of adjoint fermions in $\text{SU}(N)$ gauge theories, at zero temperature and infinite spatial volume preserves the $(\mathbb{Z}(N))^4$ symmetry related to center transformations in the four Euclidean directions. When decreasing the volume or increasing the temperature, the system can go through various phase regimes with different center symmetry patterns. Phase transitions could also occur as we move along the parameter space of our theory, that is to say when altering β and am.

Center symmetry breaking can be investigated by studying the corresponding order parameter. The order parameter for the center symmetry behavior along the direction $\hat{\mu}$ is the vacuum expectation value of the traced Polyakov loop in that direction,

$$P_\mu = \frac{1}{N} \sum_{x_\perp} \text{Tr}\left(\prod_{i=0}^{L_\mu-1} U_\mu(x_\perp, x_i) \right), \qquad (11)$$

where x_i is the coordinate along the μth direction, $x_\perp$ is the set of coordinates in the perpendicular directions to $\hat{\mu}$, and L_μ is the number of lattice points in the $\hat{\mu}$ direction. The temporal direction is denoted by $\mu = 0$, while the three spatial directions are denoted by $\mu = 1, 2, 3$.

For large enough physical lattice volume, the center symmetry should be unbroken, and the distribution of P_μ along all directions should show a single peak at zero. This pattern will change as we reduce the lattice size. In a center symmetry broken phase, at smaller lattices, N peaks will start to appear in one of the Polyakov loop distributions. However, more complicated breaking patterns are possible for fermions in the adjoint representation depending on lattice volume and boundary conditions. A single phase transition to a deconfined phase with broken center

symmetry[4] is expected only in the case of thermal boundary conditions, different intermediate phases can occur, and a reconfined phase with unbroken center symmetry is observed if the lattice size in one direction becomes very small [46]. The intermediate phases might even be absent at small fermion masses as observed in super-Yang-Mills theory [47,48].

We consider periodic boundary conditions in all spacial directions, and the significantly larger temporal direction can be neglected in this consideration. None of the ensembles shows any indications for center symmetry breaking. To demonstrate this, in Fig. 1, we present histograms of the vacuum expectation value of Polyakov loops along all four directions for the ensembles DB1M10, DB2M7, DB3M8, and DB4M11. These are the configurations which correspond to the four values of β and the smallest mass for each.

In order to exclude any possibility that this signal might accidentally be due to a reconfined phase not connected to confinement at large volume, we have done some additional investigations. In such a phase, center symmetry breaking is expected when the periodic boundary conditions are changed to thermal ones. We have confirmed, in additional simulations using thermal boundary conditions, that these small-volume effects are absent in our calculations.

B. Topological aspects

The second important aspect that needs to be considered in order to check the validity of the considered parameter range is topological charge fluctuations of the ensembles. Our simulations should be ergodic and hence effectively explore all topological sectors. In Monte Carlo simulations based onHybrid Monte Carlo (HMC) algorithms, strong autocorrelations of the topological charge appear as one approaches the continuum limit. This well-known phenomenon of topological freezing has to be excluded for the extended $\beta - am$ parameter space that we are considering in our current simulations.

In the continuum, the topological charge Q is defined as the integral over the four-dimensional volume of the topological charge density

$$Q = \frac{1}{32\pi^2} \int d^4 x \epsilon_{\mu\nu\rho\sigma} \text{Tr}[G_{\mu\nu}(x) G_{\rho\sigma}(x)]. \tag{12}$$

The discretized lattice counterpart of the above quantity can be obtained by replacing the gluonic field strength with a lattice operator that reproduces the correct continuum limit. The choice is not unique, and operators with

---

[4]Thermal boundary conditions refers to periodic boundary conditions for all fields, except for the fermions. These have antiperiodic boundary conditions in one direction with the smallest extend corresponding to the inverse temperature.
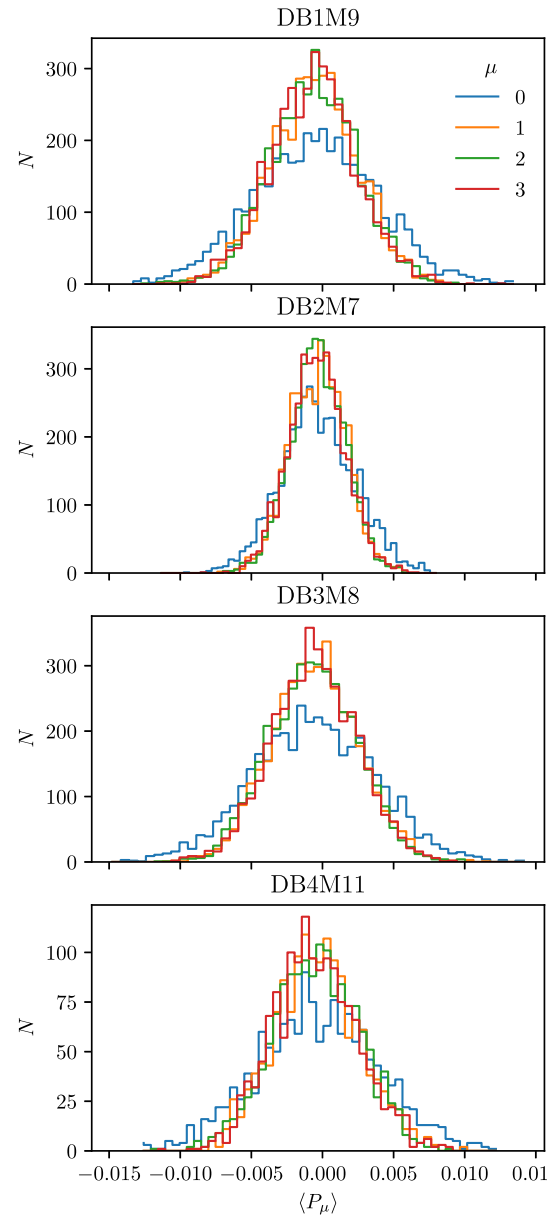

FIG. 1.   The histograms of the average Polyakov loop for the ensembles DB1M10, DB2M7, DB3M8, and DB4M11 belonging to the set shown in the label of each subfigure, for the four space-time directions. Single peaks indicate an unbroken center symmetry.

better finite-size effects can be obtained by using $O(a)$-improved discretizations of the field strength. For the purposes of this work, we incorporated the so-called "clover" definition,

$$Q_L = \frac{1}{32\pi^2} \sum_x \epsilon_{\mu\nu\rho\sigma} \text{Tr}[C_{\mu\nu}(x) C_{\rho\sigma}(x)], \tag{13}$$

where the "clover leaf" $C_{\mu\nu}$ corresponds to the sum of the plaquettes $P_{\mu\nu}(x)$ centered in x and with all the possible orientations in the $\mu\nu$-plane. This operator is even under

parity transformations and exhibits $\mathcal{O}(a^2)$ discretization effects. After a certain smoothing of the gauge configurations, Q tends to integer values labeling the topological sector for each gauge configuration.

Smoothing is required to suppress ultraviolet fluctuations of the gauge fields that would contaminate measurements of Q. We use the gradient flow [49] with the standard Wilson action to implement it.[5]

To monitor possible effects of topological freezing and, thus, a loss of ergodicity, we investigate the Monte Carlo history and the histogram of the topological charge for several different parameters. In Fig. 2, we present the Monte Carlo history of the topological charge Q for the ensembles DB1M10, DB2M7, DB3M8, and DB4M11 with the corresponding histogram. These ensembles correspond to the smallest fermion masses at the four different values of β. One can observe that for none of the ensembles is an extreme autocorrelation time of Q observed, and topological freezing is hence not a problem in the considered parameter range. A large number of topological sectors are explored, and the resulting histogram is compatible with a Gaussian distribution with average at zero. This is a strong indication for a adequate sampling of topological observables. Full results for the autocorrelation time, and for the fitted shape of the histogram of Q, are shown in Appendix B.

Besides the check for the reliability of the simulations, this study provides also further insights into the physical properties of the theory. The topological susceptibility χ,

$$\chi = \frac{\langle Q^2 \rangle - \langle Q \rangle^2}{V}, \tag{14}$$

provides information about the possible IR conformal scenario for the theory.

An IR conformal theory becomes confining when deformed by a fermion mass. If this occurs, the theory should be indistinguishable from the equivalent quenched theory. A good quantity to test this scenario is the topological susceptibility, since it should match the pure SU(2) Yang-Mills theory [50] results.

In Fig. 3, we present the topological susceptibility in units of the string tension $\chi^{\frac{1}{4}}/\sqrt{\sigma}$ as a function of the string tension in lattice units $a^2\sigma$. This is compared to the same quantity in pure SU(2) Yang-Mills theory corresponding to the quenched $N_f = 0$ case. Furthermore, the result for the $N_f = 2$ case is shown, which is expected to be IR conformal. The topological susceptibility is in good agreement between these three theories; any discrepancies are
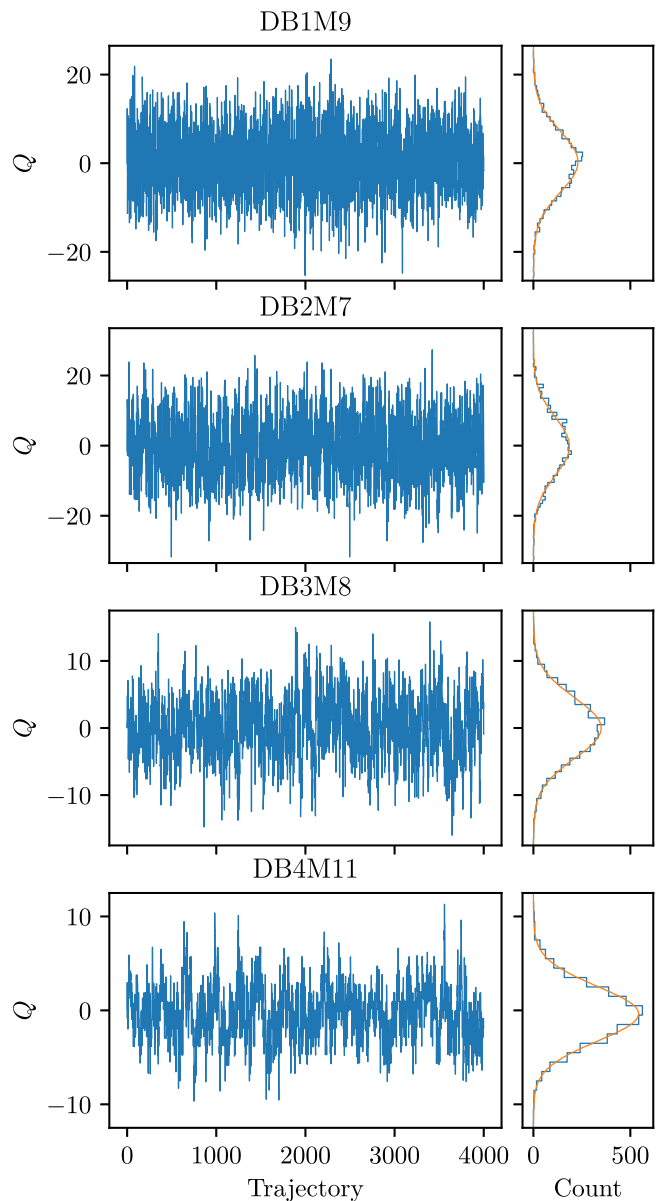

FIG. 2. Monte Carlo history of Q (left panel) and resulting histogram (right panel) computed on 4000 configurations extracted using gradient flow at gradient flow time τ corresponding to $a\sqrt{8\tau_{\text{flow}}} = L/2$ for the ensembles DB1M10, DB2M7, DB3M8, and DB4M11.

understood as higher-order scaling corrections of $a^2\sigma$. This provides a first indication that SU2Nf1Adj is IR conformal.

The gradient flow also enables the definition of scale parameters t_0 and w_0, which can be determined quite accurately to high precision. These flow observables were introduced in Refs. [51,52]. t_0 is defined according to the following prescription. First, we set

$$F(t) = t^2 \langle E(t) \rangle \quad \text{where} \quad E(t) = \frac{1}{4} B_{\mu\nu}^2(t), \tag{15}$$

---

[5]The elementary integration step is ($\epsilon = 0.01$). The flow time t is chosen large enough to cancel discretization effects while still keeping the topological content of the gauge fields unchanged. For this reason, we extracted the topological charge for flow times ($\tau_{\text{flow}} = t_{\text{flow}}/a$) corresponding to $\sqrt{8t_{\text{flow}}} = L/2$.
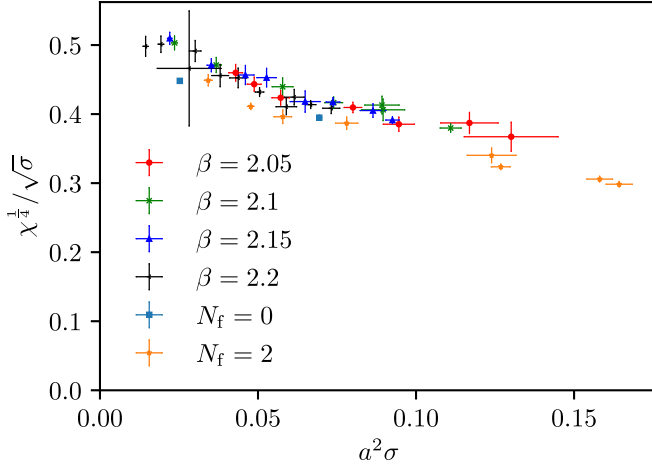
FIG. 3. The topological susceptibility measured for the largest combination of each (β, m), in units of the string tension $\sqrt{\sigma}$. Included for comparison are data for pure SU(2) gauge theory and the SU(2) theory with two adjoint Dirac flavors, using data from Ref. [50].

where $B_{\mu\nu}$ is field strength obtained by flowing $G_{\mu\nu}$ along the flow time direction. We identify the scale t_0 as the value of t for which

$$F(t)|_{t=t_0(c)} = c. \qquad (16)$$

Similarly, w_0 is defined by

$$t\frac{\mathrm{d}}{\mathrm{d}t}F(t)|_{t=w_0^2(c)} = c. \qquad (17)$$

In these definitions, c is chosen such that the relevant condition $a \ll \sqrt{8t_0} \ll L$ or $a \ll \sqrt{8w_0} \ll L$ is satisfied. Small c lead to larger lattice artifacts, and larger c usually lead to larger autocorrelations [53]. In our case, we take $c = 0.2$ consistent with the common value of $c = 0.3$ for QCD assuming a scaling with N as in Ref. [54]. $G_{\mu\nu}$ is represented by the clover plaquette.

C. Particle spectrum

The first important observables which we consider to determine conformal or confining infrared behavior are the masses of the particles. We considered masses of mesonic and baryonic two-fermion states, glueballs, and a spin-$\frac{1}{2}$ hybrid fermion state. In addition, we have determined string tension and scale setting quantities (w_0 and t_0). In this section we first discuss basic features of these data, which are later on considered in more detailed fits according to a conformal or confining scenario. In the current work, we focused on the most precise data and excluded two-fermion states with disconnected contributions. Our methodology for determining the masses follows very closely our previous work [36].

The data are summarized in Appendix B and represented in units of w_0 in Figs. 4 and 5. In order to control finite-volume effects, we have included different volumes for some parameters.

Several important observations can already be made from this representation of the data. As observed in our previous study, there is only a small dependence of the masses in physical units on the PCAC mass which becomes more profound as β and PCAC mass increase. This is consistent with the expectation for a conformal theory. In such a case, masses of states and quantities used for scale setting tend to zero in the chiral limit, i.e., as $m_{\mathrm{PCAC}} \to 0$, with the same exponent, leading to constant mass ratios and constant masses in units of w_0.

At small PCAC masses, there is still a considerable deviation from the expected constant behavior. In particular, the scalar baryon (γ_5 channel), which should become Goldstone boson in case of chiral symmetry breaking, tends toward smaller masses. However, this trend is reduced at larger values of β and might hence be related to lattice

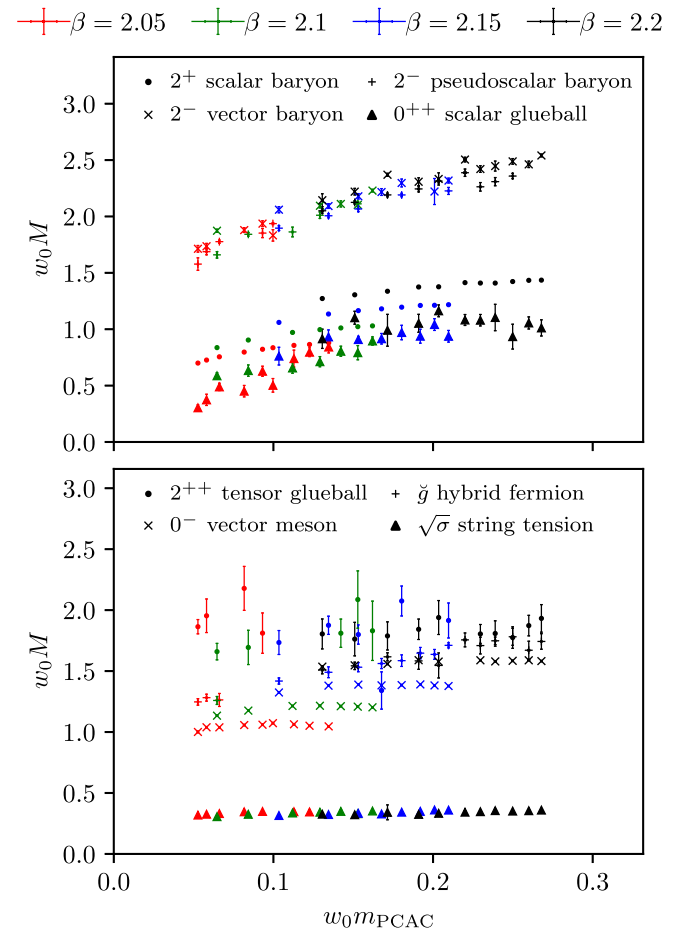FIG. 4. The mass spectrum observed at the largest volume for each combination of (β, m), showing baryons, glueballs, the hybrid fermion $\breve{g}$, and the string tension $\sqrt{\sigma}$, as a function of the PCAC fermion mass, in units of the gradient flow scale w_0.
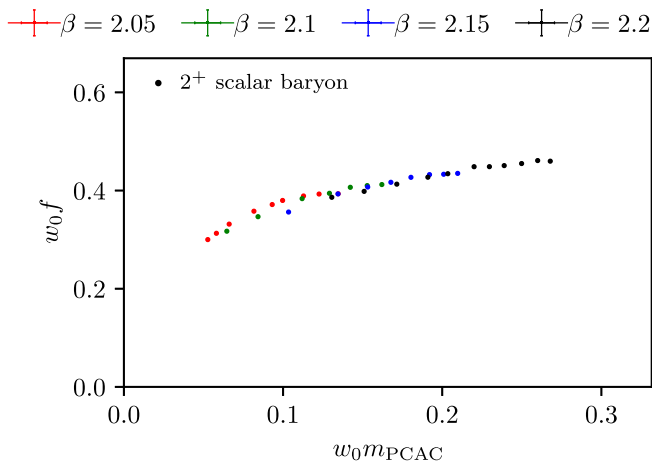
FIG. 5. The decay constant of the 2^+ baryon observed at the largest volume for each combination of (β, m), as a function of the PCAC fermion mass, in units of the gradient flow scale w_0.

artifacts. More detailed considerations are therefore required to resolve the continuum behavior of the theory.

The ordering of the states in the particle spectrum provides further insight into possible infrared scenarios for the theory. Different from a chiral symmetry breaking scenario, the scalar glueball is the lightest state of the theory, lighter than the 2^+ scalar baryon at all points observed, as shown in Fig. 6. A light glueball is also observed in several near-conformal theories, and might even be related to a dilaton state in the conformal limit. The spin-$\frac{1}{2}$ hybrid fermion state is rather light compared to other baryonic and mesonic states. However, it is still heavier than the scalar glueball and scalar baryon. Therefore, our results rather indicate that the discussed exotic infrared scenario conjectured in Refs. [3,4] with light baryon states is not realized for this theory.
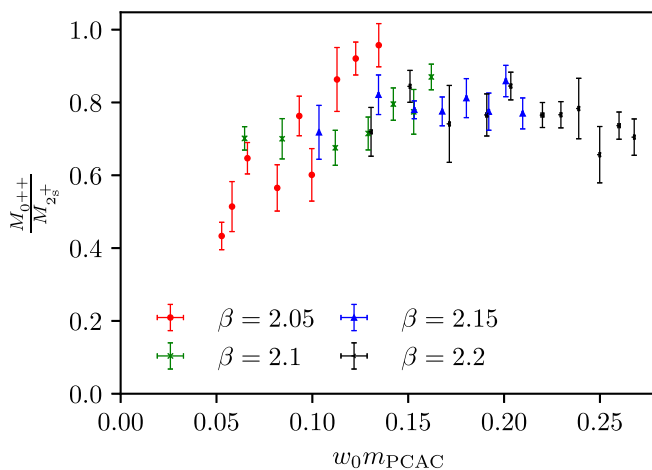

FIG. 6. The ratio of the mass of the 0^{++} glueball to that of the 2^+ scalar baryon as a function of the PCAC fermion mass scaled by the gradient flow scale w_0.

D. Determination of the mass anomalous dimension for the different gauge couplings

We continue the analysis considering an IR conformal scenario of SU2Nf1Adj. In such a scenario, the scaling of relevant observables is governed by the mass anomalous dimension at the IR fixed point γ_*. In the following, we consider two methods for the determination of the scaling. The first one is a hyperscaling analysis of the particle spectrum. The second one considers the scaling of the mode number, the integrated eigenvalue density of the Dirac operator. Consistent fits are a good indication for the realization of a conformal scenario. In this section, we first analyze separately the different values of the gauge coupling. A final result of this quantity at the fixed point would be independent of the gauge coupling. In the last part, we consider possible ways to determine the universal scaling based on the data of the complete parameter range.

In our previous investigation, we have determined the value at a single $\beta = 2.05$ [36]. This value is updated with additional ensembles at the same gauge coupling.

1. Particle spectrum

Near-conformal behavior would indicate a particular scaling of the particle masses. Including the approximate finite-size effects, a spectral quantity M as a function of the m_{PCAC} mass follows the scaling relation [21,22,55–59]

$$LaM = f(L(am_{\mathrm{PCAC}})^{\frac{1}{1+\gamma_*}}), \qquad (18)$$

for some function f, where $L \to \infty$ is the finite spatial extent of the lattice. This implies that the points in a plot of LaM against $L(am_{\mathrm{PCAC}})^{1/(1+\gamma_*)}$ collapse to one universal curve for the correct value of γ_*.

These plots, based on the data for the scalar baryon, are shown in Fig. 7. In a certain range of γ_*, the values for all gauge couplings become nearly consistent with a universal function. In order to perform a more precise determination, we have applied the methodology proposed by DeGrand [56] based on work by Bhattacharjee and Seno [60]. The principle of this method is to allow the data to shape the fit function, rather than imposing a fitting form. This is done by minimization of the function

$$P(\gamma_*) = \frac{1}{N_o} \sum_{\ell \in \{L\}} \sum_{i \in S_\ell} (L_i aM_i - f_\ell(L_i^{1+\gamma_*} am_{\mathrm{PCAC}i}))^2, \quad (19)$$

where S_ℓ is the set of data such that for $i \in S_\ell$, $L_i \neq \ell$, and $L_i^{1+\gamma_*} am_{\mathrm{PCAC}i}$ is in the range spanned by the data for which $L = \ell$, and N_o is the number of points i considered in total, i.e., $N_o = \sum_{\ell \in \{L\}} \sum_{i \in S_\ell} 1$. f_ℓ is a function interpolating the values of LaM for data for which $L = \ell$; we choose this interpolation to be piecewise linear. This minimization
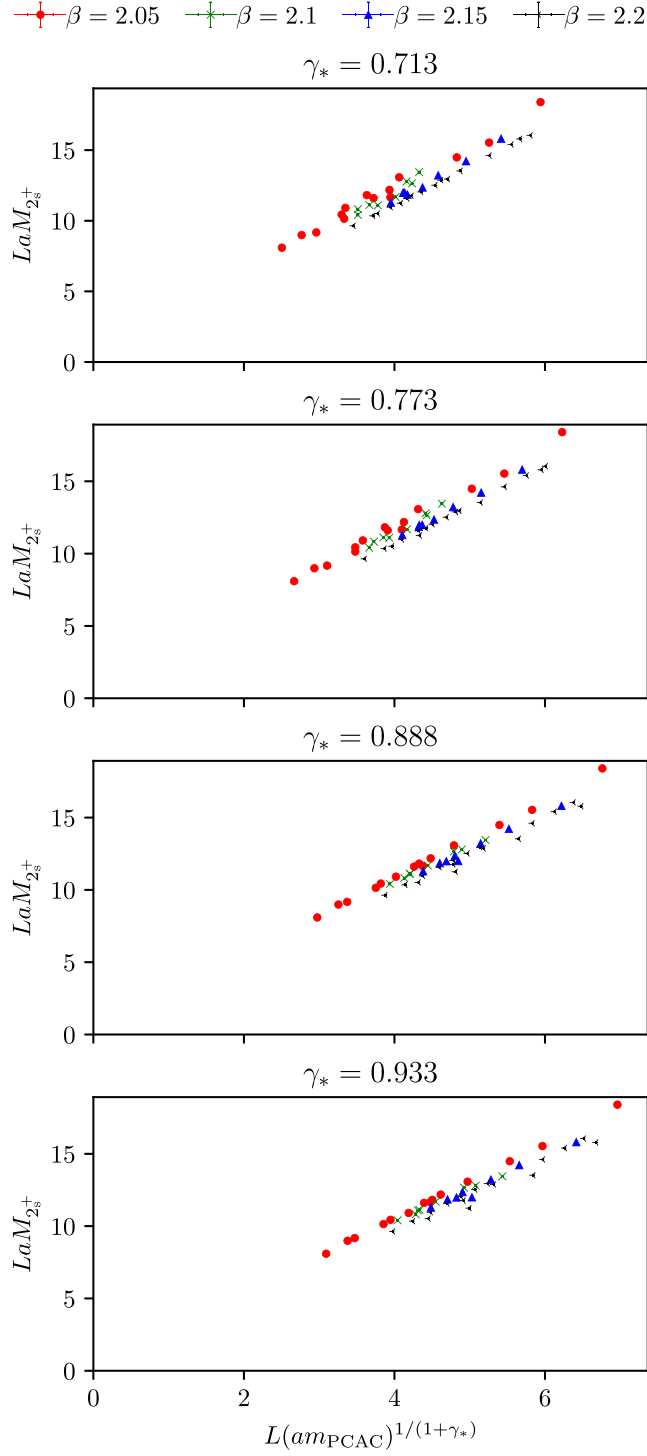
FIG. 7.   Finite-size hyperscaling plots showing the mass of the 2^+ baryon as a function of the product $Lm_{\text{PCAC}}^{1/(1+\gamma_*)}$ for the stated values of γ_*. Data for different values of β align at different values of γ_*, with the extrema being $\beta = 2.05$ data aligning at $\gamma_* = 0.943(71)$ and $\beta = 2.2$ data aligning at $\gamma_* = 0.717(43)$.

pulls the data for each value of L to the others, collapsing the data to a single global function without needing to specify its functional form.

TABLE I.   Results of fitting the anomalous dimension γ_* from finite-size hyperscaling using the methodology described in Refs. [56,60]. N_{points} is the total number of points contributing to the residual at the given value for γ_*.

β	γ_*	N_{points}
2.05	0.933(71)	14
2.1	0.89(12)	4
2.15	0.773(47)	7
2.2	0.713(43)	20

This detailed analysis reveals more significant deviations between γ_* obtained at different values of the gauge coupling β. As shown in Table I, smaller values of γ_* are preferred at larger β.

2. Mode number

The eigenvalue spectrum of the Dirac operator allows a more precise determination of γ_* compared to the scaling of the particle spectrum. We have already described the method in Ref. [36]. The integrated eigenvalue density $\bar{\nu}(\Omega)$ or mode number as a function of upper integration limit Ω follows in an intermediate regime the scaling

$$a^{-4}\bar{\nu}(\Omega) \approx a^{-4}\bar{\nu}_0(\tilde{m}) + A[(a\Omega)^2 - (a\tilde{m})^2]^{\frac{2}{1+\gamma_*}}, \quad (20)$$

where $\tilde{m}$ is some renormalized fermion mass [61,62].

To find the region of validity, we have used several different windows $[\Omega_{\text{LE}}, \Omega_{\text{UE}}]$ for the fit according to the scaling formula (20). The numerical fit and the specific functional form leads to an additional dependence of the results on the initial parameters. In order to obtain an estimate of this uncertainty, many repeated fits are performed with small variations in the initial parameters around a central value. This central value is chosen by a constrained fit in which $\bar{\nu}_0 = 0$, which is significantly more stable than the full four-parameter fit. Examples of the scattering of γ_* obtained in these fits are shown in Fig. 8.

We have determined optimal values for γ_* by searching for a plateau in the distribution, constraining both Ω_{LE} and $\Delta\Omega = \Omega_{\text{UE}} - \Omega_{\text{LE}}$, and for the most reliable fits. The plateau is then fitted, weighting the result for each window both by the statistical uncertainty and also by the number of fits of that window which converged. The determination is done separately at each β, focusing in particular at the large volumes and small fermion masses. The final results are shown in Table II.

3. Universal behavior or dependency on the gauge coupling?

The obtained values of the anomalous dimension using the expected scaling of the particle spectrum or the mode number are quite consistent. The deviations of the two

TABLE II. The values of the mass anomalous dimension γ_* obtained from a fit of the mode number data according to (20).

Ensemble	Ω_{LE}^{min}	Ω_{LE}^{max}	$\Delta\Omega_{min}$	$\Delta\Omega_{max}$	γ_*
DB1M8	0.03	0.07	0.05	0.1	0.8720(52)
DB1M9	0.03	0.065	0.05	0.1	0.8743(56)
DB2M7	0.03	0.05	0.02	0.08	0.8609(83)
DB3M8	0.04	0.08	0.05	0.08	0.687(14)
DB4M11	0.05	0.09	0.05	0.09	0.575(11)

methods are between 0.2 and 3 sigma with the smallest deviation at $\beta = 2.1$ and the largest at $\beta = 2.2$. The large deviation at $\beta = 2.2$ might be seen as an indication that our determination of the scaling is not completely under control in this case. However, deviations at the order of 3 sigma between these two methods have also been observed in studies with two Dirac flavors.

An even more striking result is the dependency of γ_* on the value of β: for nearly conformal gauge theories, the fixed point value of the anomalous dimension is a universal quantity, and the gauge coupling is at most marginal. In our calculation, instead we observe that the larger β indicate a smaller value of γ_*. This may indicate that the theory is not IR conformal, despite the observed IR scaling seeming compatible at first sight with that hypothesis. However, large scaling corrections or strong lattice artifacts due to the nearby bulk transition might provide an alternative explanation. We now discuss these two possibilities.

Assuming the deviation can be explained by scaling corrections, a fit approach of Ref. [63] can be applied to quantify leading and subleading contributions. We have tried to fit our data according to this approach. However, we did not obtain consistent result since the sign of the leading exponent did not agree with the assumptions for an IR fixed point.

This leaves us with one basic interpretation of the data, which is a rather drastic correction due to the lattice artifacts. Since we have chosen our values of the gauge coupling as close to the bulk transition as possible, such effects are not unexpected. The conclusion of this line of argument is that the largest β provides the most reliable result of the conformal scaling and γ_* is smaller than estimated in our earlier work.

E. Chiral perturbation theory

In order to check the infrared scenario for the theory, the assumptions of a near-conformal scaling must be compared with the chiral symmetry breaking case. Assuming chiral symmetry breaking, the functional dependence is provided by chiral perturbation theory. We have performed a basic fit of the scalar baryon state according to this scenario. This
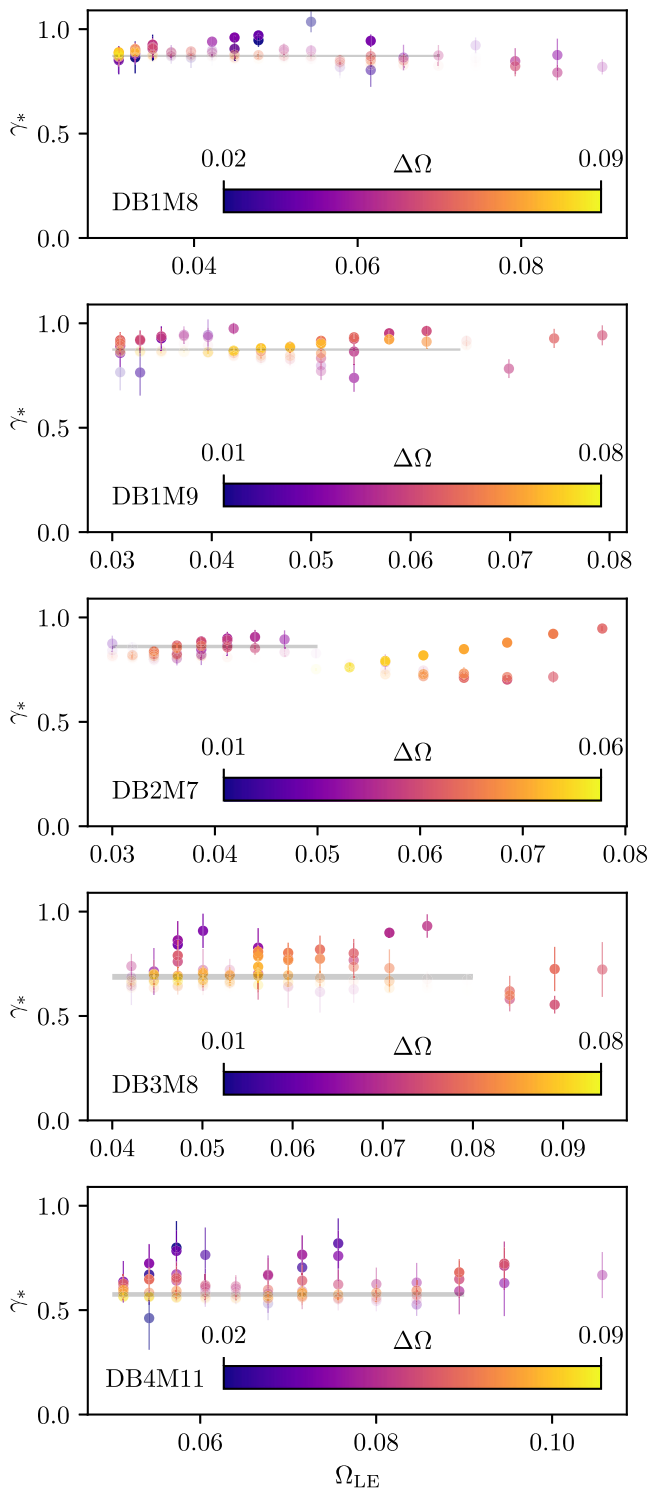
FIG. 8. Results of the bootstrapped fits of the mode number for the ensembles DB1M8, DB1M10, DB2M7, DB3M8, and DB4M11 as a function of the lower end of the fit window. Colors represent the length of the window $\Delta\Omega = \Omega_{UE} - \Omega_{LE}$, and opacity represents the proportion of fits for that window that converged.

state corresponds to the pseudo-Nambu-Goldstone boson of broken chiral symmetry.

The fit has been done according to the functional form

$$\hat{M} = 2B\hat{m}_{\text{PCAC}}(1 + L\hat{m}_{\text{PCAC}} + D_1\hat{m}_{\text{PCAC}}\log(D_2\hat{m}_{\text{PCAC}}))$$
$$+ W_1 am_{\text{PCAC}} + W_2\frac{a^2}{w_0^2}, \qquad (21)$$

where $\hat{m}_{\text{PCAC}} = w_0 m_{\text{PCAC}}$, fitting the coefficients B, L, D_1, D_2, W_1, and W_2. The result is presented in Fig. 9. It indicates rather large lattice artifacts, and the strongest deviation from the fit is seen at the largest β. Assuming the standard confinement and chiral symmetry breaking scenario, the largest β corresponds to the smallest lattice spacing.

To exclude the possibility that this fit has been anchored by the coarsest lattice spacing, where the scalar baryon mass does not exhibit the near-flat behavior observed at larger values of β, we have performed additional fits of only the finer values of the lattice spacing. This fit similarly shows very similar lattice artifacts to the fit including data at all values of β, suggesting that the inconsistency with chiral perturbation theory is a genuine effect and not an artifact of the choice of fit region.

Further simulations with larger volumes and smaller masses at this β might help to reduce the uncertainty. Overall, chiral symmetry breaking cannot be excluded from these fits. However, the complete functional dependence of the data is not well described by chiral perturbation theory. In addition, the fact that the scalar glueball is lighter than the scalar baryon is also in contradiction with chiral symmetry breaking.
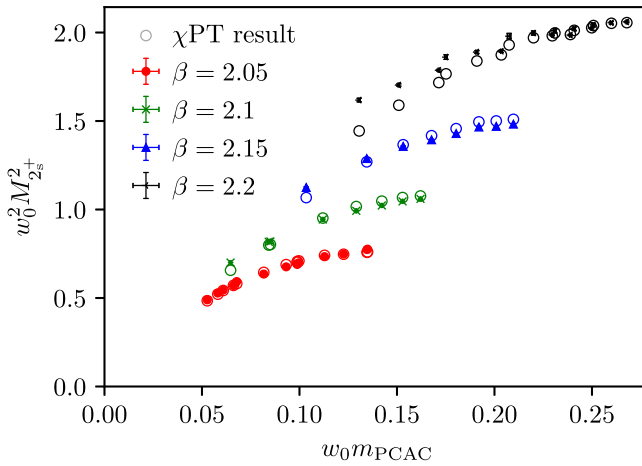

FIG. 9. The results of fitting the 2^+ baryon mass (scaled by the gradient flow scale w_0) for the largest-volume ensemble for each combination of (β, m) with chiral perturbation theory.

F. *R* ratio

In this section, we consider our new data for SU2Nf1Adj to investigate universal properties that can be used to characterize the general parameter space of strongly interacting gauge theories. In an earlier work [38], we have shown that the observable

$$R = \frac{M_{2^{++}}}{M_{0^{++}}}, \qquad (22)$$

where $M_{2^{++}}$ is the mass of the lightest spin-2 composite state and $M_{0^{++}}$ is the mass of the lightest spin-0 state, is related to the anomalous dimension γ_*. It can be used to characterize general properties of a IR conformal gauge theory. Some interesting properties make R a particularly relevant observable. More in detail, R is defined universally, can be computed explicitly for a wide range of models, is scheme independent, and it is not directly controlled by internal global symmetries of the theory. Therefore, it is legitimate to compare the value of R computed in theories with completely different internal symmetries and symmetry-breaking patterns. This is a particularly welcome feature in the context of gauge theories with fermionic field content, where the physics of chiral symmetry and its breaking introduces nontrivial model-dependent features.

Before presenting numerical results for R, we briefly review the expected behavior for a conformal theory as it is deformed by some fermion mass m. For a region of small, finite deforming mass, spectral masses will scale as $M \propto m^{1/\Delta}$, where $\Delta = 1 + \gamma_\star$ is the scaling dimension. A finite lattice volume introduces an absolute IR cutoff; thus, an appropriate scaling variable to consider is $x = Lm^{1/\Delta}$, and so the ith mass scale would become a function of x, i.e., $LM_i = f_i(x)$ as we demonstrated in Eq. (18). To first order for a state of mass M_0, this gives $LM_0 \propto x$, and by backsubstitution, we obtain $LM_i = f_i(LM_0)$. Thus, if we take mass ratios, then the dependence on the lattice extent drops out, allowing us to compare data at different volumes,

$$\frac{M_i}{M_j} = \frac{f_i(LM_0)}{f_j(LM_0)}. \qquad (23)$$

We expect that the behavior of R will be characterized by four distinct regimes. At large values of m, R becomes effectively consistent with the value seen in the pure SU(2) Yang-Mills theory; this value has been found in lattice studies to be $R = 1.44(4)$ [64,65]. At small m, the regime will depend on the lattice extent L. At large enough volumes, the observed physics shows confining properties due to the mass deformation. At very small volumes, the theory observed is that of the so-called femto-universe [38]; previous studies indicate that $R \simeq 1$ in this region [66–68]. However, there is an intermediary region of L where it is sufficiently large to observe the conformal behavior,

without being so large as to be distorted by confining effects. This is the region of interest, which can be extrapolated to a chiral limit value, allowing R to be determined for the conformal case. Since R enables comparison between disparate theories, we choose to perform a comparison with a toy model constructed making use of the principles of gauge-gravity duality [38]. This model is constructed within the bottom-up approach to holography, in such a way that the only operator deforming the theory and driving it away from conformality has scaling dimension Δ. Given our results for the anomalous dimension, we can compare the measured ratio to expectations coming from the toy model with the corresponding value of Δ. More details behind this idea can be found in our previous work [38].

In Fig. 10, we present our results on R for the four different values of the coupling β. Our data are compared with the ratio R for the SU(2) pure Yang-Mills theory (blue dashed line) as well as with the prediction from the conformal string-inspired toy model (upper band). We remark that for each different value of β the conformal prediction changes due to different measured values of γ_*. For large LM_0, the data for the four different βs moves toward the pure gauge prediction, in agreement with the discussion above. For the case of our smallest value of β, going to smaller LM_0, the calculations are becoming consistent with the conformal plateau with large R. For $\beta = 2.1$ and (to a more limited extent) for $\beta = 2.15$, there is some evidence of behavior that is different from the confining behavior, although the ratio does not rise enough to meet the value predicted by the model. At our largest value of $\beta = 2.2$, results do not move significantly above the Yang-Mills value. Further simulations are needed to confirm whether this tendency toward the confining behavior is a reflection of the physical properties of the system or the data are not in the regime that can capture IR conformality. Turning now to the regime of very small volumes, and thus smaller values of LM_0, we observe that there are no signals of "femto-universe." The above behavior is in agreement with our previous findings in Ref. [38].

Once again, we see hints of different infrared behavior at the lower and at the higher ends of the β range we have studied. In order to resolve the discrepancy, further simulations would be needed. In particular, for R, one would need to carefully design calculations that interpolate between the Yang-Mills behavior at large LM_0 and the femto-universe at lower values of this quantity, with the goal of identifying an intermediate region where infrared conformality could be visible.

IV. CONCLUSIONS

The SU(2) gauge theory with one Dirac flavor in the adjoint representation is a very interesting theory due to its relation to supersymmetric counterparts and composite Higgs models. More interestingly, there are several complementary possibilities for the corresponding effective
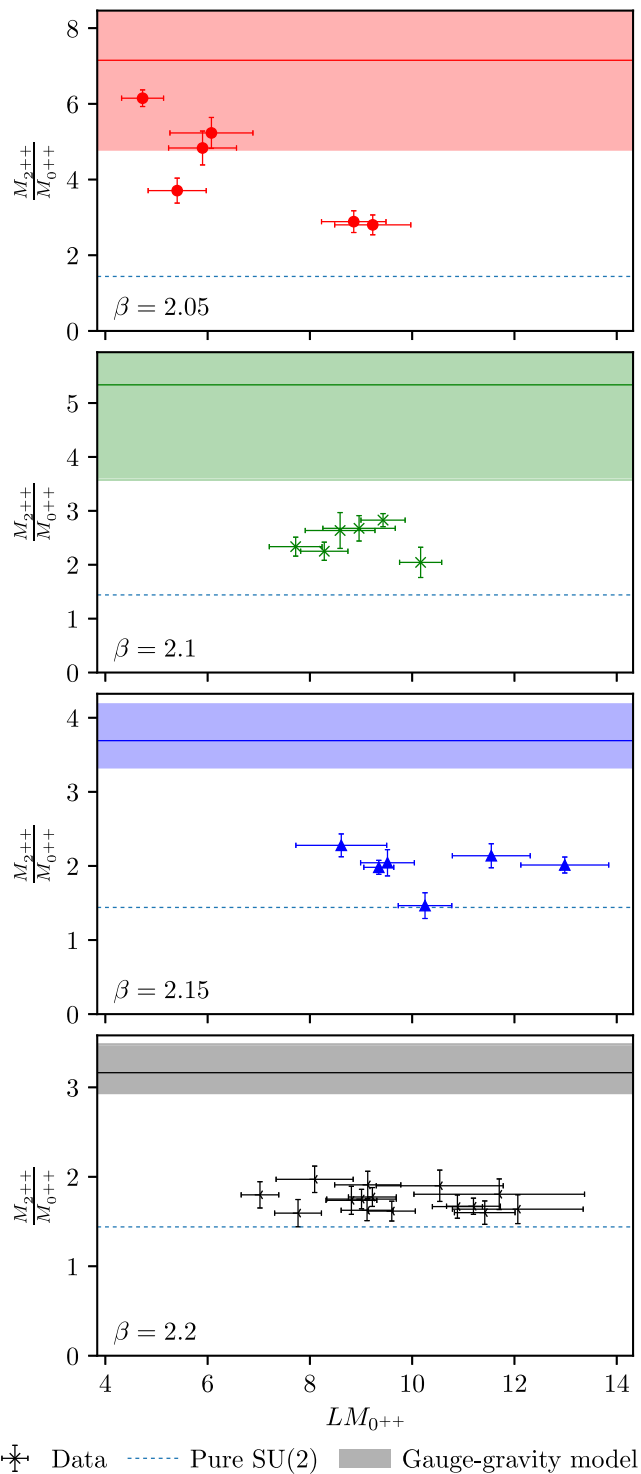
FIG. 10. The ratio $R = \frac{M_{2^{++}}}{M_{0^{++}}}$ measured at all volumes studied for each combination of (β, m). The shaded region indicates the range suggested by the model presented in Ref. [38], when the values for γ_* in Table I are used. In the case of $\beta = 2.05$ and 2.1, the upper bound on R is infinite, as γ_* is compatible with 1, at which point the model is singular.

theory in the infrared limit. It could be similar to the case with two adjoint Dirac flavors, which shows significant indications for a conformal fixed point in the infrared. It

could also follow a QCD-like scenario with chiral symmetry breaking in the infrared similar to supersymmetric Yang-Mills theory. As a third possibility, a different infrared limit has been recently suggested based on 't Hooft anomaly matching. In general, a small or even vanishing beta function is expected, which makes it rather difficult to disentangle the scenarios. From the theoretical point of view, the fact that the theory is borderline between a conformal or nonconformal case makes it an even more interesting subject. On the other hand, it provides severe challenges for the investigation on the lattice.

We have studied the theory at different lattice sizes and different values of the gauge coupling. We have investigated a large number of observables in order to characterize the infrared properties of the theory. These include the particle spectrum, topology, the Polyakov loops, and the mode number of the Dirac operator. We have confirmed the general reliability of the simulations since the gauge coupling g is chosen below the bulk transition and there is no indication for deconfinement or topological freezing. For several observables, we observe a significant dependence on the gauge coupling, which is unexpected for an infrared conformal scenario. There are basically three possible explanations:

(1) The theory is not conformal but rather QCD-like, in the infrared. Chiral symmetry is broken by a non-vanishing adjoint fermion condensate. For this conclusion, the larger deviations in the chiral fits need to be explained by lattice artifacts. It is in contradiction with the observed ordering of the particle spectrum since one would expect the Goldstone modes to be the lightest states. This could, however, be explained with too heavy fermion masses in the current simulations.

(2) The theory is conformal with scaling deviations. We are, however, currently unable to determine these violations in a reliable fit. It is in this case not completely clear which value of the gauge coupling is most reliable and brings us closest to a conformal fixed point.

(3) The theory is conformal, but the influence of the bulk phase is stronger than expected. In this case, one would prefer the largest β, and consequently, a smaller mass anomalous dimension would be obtained.

While not fully conclusive, our calculations based primarily on the ordering of the scalar baryon vs the scalar glueball (Fig. 6) seem to disfavor scenario 1, therefore hinting toward the IR (near-)conformality of the theory. However, given the dependence of the mass anomalous dimension on the coupling, further investigations at large β and at smaller fermion masses are needed in order to fully answer the question of the phase realized by the theory.

Concerning the suggested alternative scenario based on 't Hooft anomaly matching, we can provide some indications that it might not be realized in the infrared. In this case, one would expect that the spin-$\frac{1}{2}$ hybrid fermions become the lightest states at small fermion masses. Instead, we observe that these states are of the same order as the vector meson mass and heavier than the scalar bayon and the scalar glueball.

ACKNOWLEDGMENTS

APPENDIX A: LATTICE PARAMETERS

In Table III, we provide the simulation parameters used for the production of configurations on the lattices considered in this study. Here, N_{conf} indicates the number of thermalized configurations used in the averages, am is the bare fermion mass in units of the lattice spacing a, and the first column is a reference name for the set. Also indicated for each set is the lattice volume. These data are available in machine-readable format in Ref. [44].

APPENDIX B: RESULTS

In this Appendix, we collect relevant numerical results obtained in the context of this study. Namely, in Table IV, we provide results for baryonic observables; in Table V, we present results for mesonic and hybrid (spin-$\frac{1}{2}$) observables; in Table VI, we report glueball masses and the string tension; and finally, in Table VII, we present the topological properties of each ensemble; and finally, in Table VIII, we present the gradient flow scales t_0 and w_0. These data, and the raw data used to generate them, are also available in machine-readable format in Ref. [44].

TABLE III. The lattices considered in this study. Here, N_{conf} indicates the number of thermalized configurations used in the averages, am is the bare fermion mass in units of the lattice spacing a, and the first column is a reference name for the set. Also indicated for each set is the lattice volume.

	β	am	$L_0 \times L_i^3$	N_{conf}.
DB1M1	2.05	−1.475	32×16^3	4000
DB1M1*	2.05	−1.475	24×12^3	4000
DB1M2	2.05	−1.49	32×16^3	4000
DB1M3	2.05	−1.5	24×12^3	4000
DB1M4	2.05	−1.51	48×24^3	4000
DB1M4*	2.05	−1.51	32×16^3	4163
DB1M4 **	2.05	−1.51	24×12^3	4013
DB1M5	2.05	−1.514	32×16^3	4000
DB1M6	2.05	−1.519	32×16^3	4000
DB1M7	2.05	−1.523	48×24^3	4000
DB1M7*	2.05	−1.523	32×16^3	4000
DB1M8	2.05	−1.524	48×24^3	4000
DB1M8*	2.05	−1.524	32×16^3	4006
DB1M9	2.05	−1.5246	48×24^3	4000
DB2M1	2.1	−1.42	24×12^3	4000
DB2M2	2.1	−1.43	24×12^3	4000
DB2M3	2.1	−1.44	24×12^3	4000
DB2M4	2.1	−1.45	32×16^3	4000
DB2M5	2.1	−1.46	32×16^3	4000
DB2M6	2.1	−1.47	48×24^3	4000
DB2M6*	2.1	−1.47	40×20^3	4000
DB2M7	2.1	−1.474	64×32^3	4000
DB3M1	2.15	−1.35	24×12^3	4000
DB3M2	2.15	−1.36	24×12^3	4000
DB3M3	2.15	−1.37	24×12^3	4000
DB3M4	2.15	−1.38	32×16^3	4100
DB3M5	2.15	−1.39	32×16^3	4077
DB3M6	2.15	−1.4	32×16^3	4014
DB3M7	2.15	−1.41	48×24^3	4000
DB3M8	2.15	−1.422	48×24^3	4000
DB4M1	2.2	−1.28	24×12^3	8000
DB4M2	2.2	−1.29	24×12^3	4320
DB4M3	2.2	−1.3	32×16^3	4000
DB4M3*	2.2	−1.3	24×12^3	4000
DB4M4	2.2	−1.31	32×16^3	4000
DB4M4*	2.2	−1.31	24×12^3	4000
DB4M5	2.2	−1.32	32×16^3	4000
DB4M5*	2.2	−1.32	24×12^3	4000
DB4M6	2.2	−1.33	24×12^3	4092
DB4M7	2.2	−1.34	32×16^3	4000
DB4M7*	2.2	−1.34	24×12^3	4000
DB4M8	2.2	−1.35	32×16^3	4000
DB4M9	2.2	−1.36	48×24^3	4000
DB4M9*	2.2	−1.36	32×16^3	4000
DB4M10	2.2	−1.37	48×24^3	4000
DB4M11	2.2	−1.378	48×24^3	4000

TABLE IV.   Baryonic observables.

	m_{PCAC}	$am_{2_s^+}$	$af_{2_s^+}$	$am_{2_v^-}$	$af_{2_v^-}$	$am_{2_{ps}^-}$	$af_{2_{ps}^-}$
DB1M1	0.14859(18)	0.97087(27)	0.43423(54)	⋯	⋯	⋯	⋯
DB1M1*	0.14879(14)	0.97141(32)	0.43443(60)	⋯	⋯	2.251(12)	0.5919(54)
DB1M2	0.12838(40)	0.90542(58)	0.4113(14)	⋯	⋯	⋯	⋯
DB1M3	0.11135(20)	0.84527(49)	0.38375(92)	⋯	⋯	⋯	⋯
DB1M4	0.091449(85)	0.76665(15)	0.34838(27)	1.680(46)	0.319(32)	1.7763(85)	0.5197(52)
DB1M4*	0.09041(18)	0.76144(59)	0.3450(12)	⋯	⋯	⋯	⋯
DB1M4 **	0.09099(33)	0.7644(12)	0.3453(17)	⋯	⋯	⋯	⋯
DB1M5	0.08223(16)	0.72561(60)	0.3278(11)	1.709(22)	0.391(15)	1.635(36)	0.461(27)
DB1M6	0.06684(21)	0.65234(80)	0.2929(13)	1.538(17)	0.3496(97)	⋯	⋯
DB1M7	0.04770(12)	0.54480(42)	0.23919(86)	⋯	⋯	1.281(10)	0.4119(63)
DB1M7*	0.04947(36)	0.56168(91)	0.24947(92)	1.335(47)	0.302(29)	1.292(23)	0.409(14)
DB1M8	0.03938(19)	0.49236(62)	0.21206(86)	1.177(17)	0.2606(89)	1.144(18)	0.355(12)
DB1M8*	0.04171(28)	0.5058(16)	0.2190(20)	1.302(13)	0.3247(63)	⋯	⋯
DB1M9	0.03425(19)	0.45471(77)	0.1950(12)	1.113(19)	0.2487(96)	1.025(36)	0.309(26)
DB2M1	0.15326(21)	0.97363(51)	0.38982(94)	2.108(12)	0.4685(66)	⋯	⋯
DB2M2	0.13820(17)	0.92461(45)	0.37075(71)	1.901(28)	0.377(18)	1.909(20)	0.497(12)
DB2M3	0.12200(23)	0.86745(64)	0.34875(92)	1.811(23)	0.378(15)	⋯	⋯
DB2M4	0.10251(16)	0.79101(51)	0.31313(97)	1.663(15)	0.3554(87)	1.597(23)	0.421(15)
DB2M5	0.08011(19)	0.69504(63)	0.27437(70)	⋯	⋯	1.332(31)	0.340(22)
DB2M6	0.04969(12)	0.53319(48)	0.20450(67)	⋯	⋯	1.0863(95)	0.3399(62)
DB2M6*	0.05085(15)	0.54108(62)	0.20872(82)	1.119(21)	0.230(12)	1.083(21)	0.329(16)
DB2M7	0.03246(14)	0.42018(32)	0.15925(36)	0.9406(72)	0.2114(35)	0.833(14)	0.264(12)
DB3M1	0.17742(19)	1.03008(52)	0.36800(86)	1.961(18)	0.369(12)	1.884(26)	0.412(18)
DB3M2	0.16369(21)	0.98778(60)	0.35295(94)	1.810(94)	0.296(84)	⋯	⋯
DB3M3	0.14918(21)	0.94070(72)	0.3360(11)	⋯	⋯	⋯	⋯
DB3M4	0.13407(19)	0.88883(38)	0.31740(51)	1.708(26)	0.342(19)	1.628(12)	0.3969(77)
DB3M5	0.11737(15)	0.82617(44)	0.29167(75)	1.551(21)	0.293(13)	⋯	⋯
DB3M6	0.09851(17)	0.74910(52)	0.26186(81)	1.401(15)	0.2683(86)	1.329(15)	0.334(10)
DB3M7	0.07808(11)	0.65881(28)	0.22821(33)	1.214(12)	0.2238(68)	1.164(11)	0.3069(78)
DB3M8	0.04877(11)	0.49990(66)	0.1679(11)	0.971(13)	0.1936(71)	0.8940(97)	0.2643(72)
DB4M1	0.20148(14)	1.07955(38)	0.34586(59)	1.9112(94)	0.3355(54)	⋯	⋯
DB4M2	0.18925(23)	1.04361(60)	0.33566(85)	1.792(21)	0.292(13)	⋯	⋯
DB4M3	0.17617(14)	1.00319(33)	0.32081(53)	1.754(17)	0.303(11)	1.663(17)	0.338(12)
DB4M3*	0.17601(20)	1.00339(69)	0.3208(11)	1.779(18)	0.316(12)	1.710(30)	0.371(24)
DB4M4	0.16323(19)	0.96267(35)	0.30796(56)	1.672(30)	0.290(23)	1.577(25)	0.314(20)
DB4M4*	0.16340(20)	0.96441(68)	0.31073(96)	1.599(32)	0.229(19)	1.576(54)	0.314(46)
DB4M5	0.14881(18)	0.91337(40)	0.29073(65)	1.569(19)	0.262(13)	1.466(24)	0.291(19)
DB4M5*	0.14894(22)	0.91395(78)	0.2915(11)	⋯	⋯	1.559(11)	0.3622(67)
DB4M6	0.13422(24)	0.86212(93)	0.2737(12)	1.528(12)	0.2811(71)	1.457(20)	0.344(14)
DB4M7	0.11902(16)	0.80495(53)	0.25400(76)	1.364(32)	0.216(21)	1.3536(96)	0.3235(66)
DB4M7*	0.11846(26)	0.8032(11)	0.2556(13)	1.306(55)	0.185(37)	1.340(16)	0.325(10)
DB4M8	0.10217(19)	0.73539(65)	0.22852(96)	1.235(19)	0.197(11)	1.200(14)	0.2820(95)
DB4M9	0.08438(11)	0.65792(29)	0.20327(36)	1.1663(64)	0.2201(34)	1.0782(82)	0.2740(64)
DB4M9*	0.08437(18)	0.65718(85)	0.2040(11)	1.1573(91)	0.2140(47)	⋯	⋯
DB4M10	0.06517(10)	0.56358(39)	0.17199(40)	0.959(13)	0.1609(77)	0.9175(58)	0.2493(39)
DB4M11	0.04813(13)	0.46875(57)	0.14232(45)	0.790(21)	0.128(13)	0.7555(74)	0.2214(57)

TABLE V. Mesonic and hybrid (spin-$\frac{1}{2}$) observables.

	$am_{0_v^-}$	$af_{0_v^-}$	$am_{\breve{g}}$
DB1M1	1.15483(45)	0.8696(14)	$\cdots$
DB1M1*	1.15624(59)	0.8728(16)	$\cdots$
DB1M2	1.1005(11)	0.8467(33)	$\cdots$
DB1M3	1.0494(12)	0.8107(33)	$\cdots$
DB1M4	0.98420(38)	0.77328(72)	$\cdots$
DB1M4*	$\cdots$	$\cdots$	$\cdots$
DB1M4 **	0.9770(15)	0.7500(38)	$\cdots$
DB1M5	0.9353(15)	0.7030(50)	$\cdots$
DB1M6	0.8651(15)	0.6395(41)	$\cdots$
DB1M7	0.7491(16)	0.5253(35)	0.911(38)
DB1M7*	0.7707(21)	0.5625(36)	$\cdots$
DB1M8	0.7043(15)	0.4937(25)	0.869(19)
DB1M8*	0.7056(41)	0.478(10)	$\cdots$
DB1M9	0.6502(36)	0.4288(79)	0.810(17)
DB2M1	1.13767(50)	0.7691(13)	$\cdots$
DB2M2	1.09193(60)	0.7397(15)	$\cdots$
DB2M3	1.03989(71)	0.7076(16)	$\cdots$
DB2M4	0.96485(81)	0.6415(22)	$\cdots$
DB2M5	0.86843(78)	0.5705(17)	$\cdots$
DB2M6	0.6933(14)	0.4201(37)	$\cdots$
DB2M6*	0.7038(22)	0.4316(53)	0.794(27)
DB2M7	0.5694(11)	0.3328(18)	0.632(16)
DB3M1	1.16543(45)	0.6888(11)	1.448(17)
DB3M2	1.12623(60)	0.6684(15)	1.334(33)
DB3M3	1.08047(72)	0.6396(17)	1.280(36)
DB3M4	1.02976(62)	0.6069(16)	1.179(35)
DB3M5	0.96770(86)	0.5620(22)	1.093(29)
DB3M6	0.89324(95)	0.5180(20)	0.985(24)
DB3M7	0.80116(48)	0.46144(81)	0.865(26)
DB3M8	0.6244(30)	0.3274(86)	0.669(12)
DB4M1	1.18981(50)	0.6140(13)	1.311(48)
DB4M2	1.15655(56)	0.6007(14)	1.217(54)
DB4M3	1.11683(48)	0.5775(11)	1.256(49)
DB4M3*	1.11830(62)	0.5813(14)	$\cdots$
DB4M4	1.07888(48)	0.5613(11)	1.194(21)
DB4M4*	1.08156(62)	0.5680(13)	$\cdots$
DB4M5	1.02962(46)	0.5317(11)	1.108(44)
DB4M5*	1.03255(77)	0.5378(17)	1.122(42)
DB4M6	$\cdots$	$\cdots$	1.071(35)
DB4M7	0.92276(75)	0.4728(16)	0.904(60)
DB4M7*	0.9179(12)	0.4695(20)	$\cdots$
DB4M8	0.85055(80)	0.4269(17)	0.847(37)
DB4M9	0.76705(56)	0.3750(11)	0.796(16)
DB4M9*	0.76951(93)	0.3824(16)	$\cdots$
DB4M10	0.66803(51)	0.32129(82)	0.666(13)
DB4M11	0.56604(97)	0.2681(14)	0.556(12)

TABLE VI. Glueball masses and string tension.

	$a\sqrt{\sigma}$	$am_{0^{++}}$	$am_{2^{++}}$
DB1M1	$\cdots$	0.929(58)	$\cdots$
DB1M1*	0.378(19)	0.96(12)	$\cdots$
DB1M2	0.361(21)	0.834(41)	$\cdots$
DB1M3	0.342(13)	0.730(74)	$\cdots$
DB1M4	$\cdots$	0.461(55)	$\cdots$
DB1M4*	0.3092(79)	0.577(46)	1.62(13)
DB1M4 **	0.3219(74)	0.589(77)	$\cdots$
DB1M5	0.3075(80)	0.554(39)	1.60(15)
DB1M6	0.2829(49)	0.369(42)	1.78(15)
DB1M7	0.2391(58)	0.352(24)	$\cdots$
DB1M7*	0.2369(83)	0.332(32)	$\cdots$
DB1M8	0.2209(50)	0.253(34)	1.324(93)
DB1M8*	0.2174(53)	0.338(35)	1.25(10)
DB1M9	0.2072(53)	0.197(17)	1.211(38)
DB2M1	0.3331(50)	0.847(34)	1.73(23)
DB2M2	0.2987(91)	0.716(57)	1.89(21)
DB2M3	0.299(11)	0.690(38)	1.55(10)
DB2M4	0.2719(52)	0.565(36)	$\cdots$
DB2M5	0.2404(69)	0.469(33)	$\cdots$
DB2M6	0.1918(43)	0.373(29)	0.999(83)
DB2M6*	0.1930(31)	0.386(26)	0.902(64)
DB2M7	0.1536(30)	0.295(13)	0.833(34)
DB3M1	0.3042(35)	0.793(44)	1.62(12)
DB3M2	0.2939(69)	0.848(43)	$\cdots$
DB3M3	0.2715(40)	0.729(48)	$\cdots$
DB3M4	0.2548(93)	0.722(48)	1.543(91)
DB3M5	0.2296(67)	0.641(33)	0.94(11)
DB3M6	0.2145(64)	0.584(18)	1.157(51)
DB3M7	0.1877(36)	0.541(36)	1.089(43)
DB3M8	0.1486(24)	0.359(37)	0.818(46)
DB4M1	0.2705(50)	0.761(54)	1.453(85)
DB4M2	0.2582(32)	0.768(39)	1.364(61)
DB4M3	0.2479(64)	0.659(78)	1.251(62)
DB4M3*	0.2444(63)	0.800(38)	1.294(74)
DB4M4	0.2428(67)	0.754(80)	1.235(71)
DB4M4*	0.2346(77)	0.760(42)	1.235(71)
DB4M5	0.2247(30)	0.700(33)	1.169(50)
DB4M5*	0.2282(39)	0.734(41)	1.28(10)
DB4M6	0.2091(65)	0.660(30)	$\cdots$
DB4M7	0.1950(68)	0.680(31)	1.134(81)
DB4M7*	0.1919(53)	0.585(31)	1.053(80)
DB4M8	0.1736(53)	0.563(43)	0.986(45)
DB4M9	0.168(30)	0.488(70)	0.880(57)
DB4M9*	0.1598(39)	0.485(29)	0.774(70)
DB4M10	0.1389(32)	0.476(25)	0.761(59)
DB4M11	0.1202(34)	0.337(31)	0.665(45)

TABLE VII. Properties of the topological charge distribution of each ensemble. Q_0 denotes the average value of the topological charge Q, and σ_Q denotes the width of the distribution of Q.

	Q_0	σ_Q	$\tau_{\exp}$
DB1M1	−0.36(10)	6.318(75)	2.03(19)
DB1M1*	−0.124(61)	3.766(44)	1.018(57)
DB1M2	0.01(10)	6.273(74)	2.18(14)
DB1M3	−0.014(57)	3.549(41)	1.394(70)
DB1M4	0.04(18)	11.02(13)	1.397(88)
DB1M4*	0.034(88)	5.475(65)	3.06(28)
DB1M4 **	0.108(51)	3.207(37)	2.98(23)
DB1M5	0.045(82)	5.065(59)	2.68(22)
DB1M6	0.139(78)	4.839(57)	3.69(28)
DB1M7	−0.02(13)	8.22(10)	1.80(10)
DB1M7*	0.065(65)	4.037(47)	1.88(15)
DB1M8	−0.20(12)	7.592(89)	1.84(14)
DB1M8*	0.076(60)	3.717(44)	4.39(42)
DB1M9	0.17(12)	7.258(87)	0.993(39)
DB2M1	0.027(52)	3.240(38)	1.554(74)
DB2M2	−0.192(50)	3.078(35)	1.554(72)
DB2M3	0.001(47)	2.950(33)	1.91(12)
DB2M4	0.034(75)	4.617(55)	2.10(14)
DB2M5	0.021(65)	4.018(47)	2.09(16)
DB2M6	−0.43(11)	6.501(81)	3.29(27)
DB2M6*	−0.238(74)	4.574(51)	2.84(21)
DB2M7	−0.22(14)	8.338(97)	2.05(14)
DB3M1	0.139(46)	2.890(33)	2.04(15)
DB3M2	−0.033(46)	2.827(32)	2.41(11)
DB3M3	0.031(42)	2.612(30)	2.52(16)
DB3M4	0.201(66)	4.099(48)	2.34(20)
DB3M5	0.196(63)	3.888(45)	2.36(15)
DB3M6	0.044(56)	3.470(41)	2.75(15)
DB3M7	−0.13(10)	6.299(76)	3.53(22)
DB3M8	−0.048(75)	4.609(54)	5.13(34)
DB4M1	−0.015(28)	2.482(20)	2.71(18)
DB4M2	0.094(37)	2.315(25)	2.70(16)
DB4M3	0.124(64)	3.982(46)	3.13(23)
DB4M3*	−0.113(35)	2.187(25)	2.74(14)
DB4M4	−0.089(58)	3.585(42)	3.30(27)
DB4M4*	−0.008(37)	2.281(26)	3.69(18)
DB4M5	0.077(55)	3.402(40)	3.65(28)
DB4M5*	0.105(34)	2.107(23)	4.63(33)
DB4M6	0.040(30)	1.870(20)	3.80(26)
DB4M7	0.048(46)	2.881(32)	3.98(24)
DB4M7*	−0.147(29)	1.801(20)	4.56(24)
DB4M8	−0.009(43)	2.667(30)	4.93(30)
DB4M9	−0.145(79)	4.888(57)	6.28(35)
DB4M9*	−0.248(36)	2.256(26)	5.70(35)
DB4M10	−0.124(64)	3.908(44)	6.42(35)
DB4M11	−0.358(48)	2.958(35)	7.97(49)

TABLE VIII. The t_0 and w_0 scales for each ensemble, in lattice units. The superscript "plaq." and "sym." refer to the definitions of the density E from the single plaquette and from the symmetrised four-plaquette clover operator respectively. w_0^{sym} here is the scale used as w_0 elsewhere in the text.

	$\sqrt{8t_0^{\text{plaq}}}/a$	$\sqrt{8t_0^{\text{sym}}}/a$	w_0^{plaq}/a	w_0^{sym}/a
DB1M1	2.21398(51)	2.80942(51)	0.88342(34)	0.90605(28)
DB1M1*	2.21564(69)	2.81033(68)	0.88450(43)	0.90688(42)
DB1M2	2.34765(75)	2.92049(70)	0.93640(41)	0.95515(35)
DB1M3	2.5089(20)	3.0526(16)	0.99676(85)	1.01351(67)
DB1M4	2.73611(53)	3.23634(51)	1.07282(30)	1.09027(26)
DB1M4*	2.7457(18)	3.2445(16)	1.07669(84)	1.09406(79)
DB1M4 **	2.7202(32)	3.2240(28)	1.0693(15)	1.0863(14)
DB1M5	2.8665(20)	3.3418(18)	1.11523(82)	1.13312(96)
DB1M6	3.1344(36)	3.5664(31)	1.2028(13)	1.2220(13)
DB1M7	3.6132(17)	3.9879(15)	1.36604(68)	1.38643(63)
DB1M7*	3.5669(42)	3.9462(34)	1.3514(16)	1.3712(16)
DB1M8	3.8718(23)	4.2228(21)	1.45400(86)	1.47563(83)
DB1M8*	3.8220(66)	4.1766(65)	1.4392(26)	1.4596(27)
DB1M9	4.0656(22)	4.3985(20)	1.51666(81)	1.53894(89)
DB2M1	2.5678(19)	3.0749(16)	1.03867(87)	1.05742(76)
DB2M2	2.7229(23)	3.1988(20)	1.0873(10)	1.10611(93)
DB2M3	2.9105(28)	3.3536(22)	1.1458(12)	1.1659(11)
DB2M4	3.2950(21)	3.6840(19)	1.23910(95)	1.25959(88)
DB2M5	3.7156(37)	4.0556(34)	1.3760(15)	1.3977(16)
DB2M6	4.6124(30)	4.8842(33)	1.6714(13)	1.6956(15)
DB2M6*	4.5505(39)	4.8252(41)	1.6496(17)	1.6732(16)
DB2M7	5.4980(31)	5.7318(31)	1.9644(12)	1.9917(12)
DB3M1	3.0042(26)	3.4138(27)	1.1608(13)	1.1820(13)
DB3M2	3.1483(34)	3.5364(31)	1.2058(14)	1.2273(15)
DB3M3	3.3224(43)	3.6910(40)	1.2657(19)	1.2871(19)
DB3M4	3.6002(29)	3.9360(27)	1.3225(12)	1.3451(10)
DB3M5	3.8580(31)	4.1673(31)	1.4070(14)	1.4291(13)
DB3M6	4.2426(43)	4.5212(43)	1.5320(18)	1.5549(17)
DB3M7	4.7560(34)	5.0023(28)	1.6987(13)	1.7227(12)
DB3M8	5.9555(75)	6.1593(81)	2.0940(32)	2.1213(29)
DB4M1	3.5912(30)	3.9135(30)	1.3071(14)	1.3295(14)
DB4M2	3.7187(50)	4.0295(51)	1.3511(22)	1.3737(23)
DB4M3	3.8608(32)	4.1583(29)	1.3951(14)	1.4183(14)
DB4M3*	3.8733(50)	4.1690(51)	1.4026(25)	1.4247(22)
DB4M4	4.0069(36)	4.2904(36)	1.4400(15)	1.4638(16)
DB4M4*	4.0230(66)	4.3061(65)	1.4512(31)	1.4743(32)
DB4M5	4.2441(44)	4.5096(39)	1.5203(19)	1.5432(17)
DB4M5*	4.2569(78)	4.5225(83)	1.5277(43)	1.5509(40)
DB4M6	4.507(11)	4.759(11)	1.6153(51)	1.6392(45)
DB4M7	4.7605(66)	4.9929(58)	1.6868(25)	1.7098(25)
DB4M7*	4.836(13)	5.070(13)	1.7279(56)	1.7517(66)
DB4M8	5.2149(89)	5.4324(85)	1.8448(37)	1.8692(35)
DB4M9	5.7286(60)	5.9249(56)	2.0061(25)	2.0319(28)
DB4M9*	5.819(14)	6.013(15)	2.0516(66)	2.0759(67)
DB4M10	6.5742(97)	6.7521(96)	2.2901(41)	2.3159(39)
DB4M11	7.728(18)	7.891(19)	2.6863(78)	2.7139(75)

[1] M. Ünsal, Magnetic bion condensation: A New mechanism of confinement and mass gap in four dimensions, Phys. Rev. D **80**, 065001 (2009).

[2] G. Basar, A. Cherman, D. Dorigoni, and M. Ünsal, Volume Independence in the Large N Limit and an Emergent Fermionic Symmetry, Phys. Rev. Lett. **111**, 121601 (2013).

[3] Z. Bi and T. Senthil, Adventure in Topological Phase Transitions in 3 + 1-D: Non-Abelian Deconfined Quantum Criticalities and a Possible Duality, Phys. Rev. X **9**, 021034 (2019).

[4] M. M. Anber and E. Poppitz, Two-flavor adjoint QCD, Phys. Rev. D **98**, 034026 (2018).

[5] S. Weinberg, Implications of dynamical symmetry breaking, Phys. Rev. D **13**, 974 (1976); **19**, 1277(A) (1979).

[6] L. Susskind, Dynamics of spontaneous symmetry breaking in the Weinberg-Salam theory, Phys. Rev. D **20**, 2619 (1979).

[7] E. Eichten and K. D. Lane, Dynamical breaking of weak interaction symmetries, Phys. Lett. **90B**, 125 (1980).

[8] B. Holdom, Raising the sideways scale, Phys. Rev. D **24**, 1441 (1981).

[9] B. Holdom, Techniodor, Phys. Lett. **150B**, 301 (1985).

[10] K. Yamawaki, M. Bando, and K.-I. Matumoto, Scale Invariant Technicolor Model and a Technidilaton, Phys. Rev. Lett. **56**, 1335 (1986).

[11] T. W. Appelquist, D. Karabali, and L. Wijewardhana, Chiral Hierarchies and the Flavor Changing Neutral Current Problem in Technicolor, Phys. Rev. Lett. **57**, 957 (1986).

[12] M. E. Peskin and T. Takeuchi, Estimation of oblique electroweak corrections, Phys. Rev. D **46**, 381 (1992).

[13] F. Sannino and M. Shifman, Effective Lagrangians for orientifold theories, Phys. Rev. D **69**, 125004 (2004).

[14] F. Sannino and K. Tuominen, Orientifold theory dynamics and symmetry breaking, Phys. Rev. D **71**, 051901 (2005).

[15] D. D. Dietrich, F. Sannino, and K. Tuominen, Light composite Higgs from higher representations versus electroweak precision measurements: Predictions for CERN LHC, Phys. Rev. D **72**, 055001 (2005).

[16] D. D. Dietrich and F. Sannino, Conformal window of SU(N) gauge theories with fermions in higher dimensional representations, Phys. Rev. D **75**, 085018 (2007).

[17] L. Del Debbio, B. Lucini, A. Patella, C. Pica, and A. Rago, Conformal versus confining scenario in SU(2) with adjoint fermions, Phys. Rev. D **80**, 074507 (2009).

[18] A. J. Hietanen, K. Rummukainen, and K. Tuominen, Evolution of the coupling constant in SU(2) lattice gauge theory with two adjoint fermions, Phys. Rev. D **80**, 094504 (2009).

[19] S. Catterall, J. Giedt, F. Sannino, and J. Schneible, Probes of nearly conformal behavior in lattice simulations of minimal walking technicolor, arXiv:0910.4387.

[20] F. Bursa, L. Del Debbio, L. Keegan, C. Pica, and T. Pickup, Mass anomalous dimension in SU(2) with two adjoint fermions, Phys. Rev. D **81**, 014505 (2010).

[21] L. Del Debbio, B. Lucini, A. Patella, C. Pica, and A. Rago, Mesonic spectroscopy of minimal walking technicolor, Phys. Rev. D **82**, 014509 (2010).

[22] L. Del Debbio, B. Lucini, A. Patella, C. Pica, and A. Rago, The infrared dynamics of minimal walking technicolor, Phys. Rev. D **82**, 014510 (2010).

[23] F. Bursa, L. Del Debbio, D. Henty, E. Kerrane, B. Lucini, A. Patella, C. Pica, T. Pickup, and A. Rago, Improved lattice spectroscopy of minimal walking technicolor, Phys. Rev. D **84**, 034506 (2011).

[24] S. Catterall, L. Del Debbio, J. Giedt, and L. Keegan, MCRG minimal walking technicolor, Phys. Rev. D **85**, 094501 (2012).

[25] T. DeGrand, Y. Shamir, and B. Svetitsky, Infrared fixed point in SU(2) gauge theory with adjoint fermions, Phys. Rev. D **83**, 074507 (2011).

[26] S. Catterall and F. Sannino, Minimal walking on the lattice, Phys. Rev. D **76**, 034504 (2007).

[27] L. Del Debbio, A. Patella, and C. Pica, Higher representations on the lattice: Numerical simulations. SU(2) with adjoint fermions, Phys. Rev. D **81**, 094503 (2010).

[28] A. J. Hietanen, J. Rantaharju, K. Rummukainen, and K. Tuominen, Spectrum of SU(2) lattice gauge theory with two adjoint Dirac flavours, J. High Energy Phys. 05 (2009) 025.

[29] S. Catterall, J. Giedt, F. Sannino, and J. Schneible, Phase diagram of SU(2) with 2 flavors of dynamical adjoint quarks, J. High Energy Phys. 11 (2008) 009.

[30] G. Bergner, P. Giudice, G. Münster, I. Montvay, and S. Piemonte, Spectrum and mass anomalous dimension of SU(2) adjoint QCD with two Dirac flavors, Phys. Rev. D **96**, 034504 (2017).

[31] L. Del Debbio, B. Lucini, C. Pica, A. Patella, A. Rago, and S. Roman, Large-volume results in SU(2) with adjoint fermions, in *Proceedings of the 31st International Symposium on Lattice Field Theory* (Proceedings of Science, Trieste, Italy, 2013).

[32] G. Bergner, P. Giudice, G. Münster, P. Scior, I. Montvay, and S. Piemonte, Low energy properties of SU(2) gauge theory with Nf = 3/2 flavours of adjoint fermions, J. High Energy Phys. 01 (2018) 119.

[33] T. A. Ryttov and F. Sannino, Ultra minimal technicolor and its dark matter TIMP, Phys. Rev. D **78**, 115010 (2008).

[34] G. Bergner and S. Piemonte, Lattice simulations of a gauge theory with mixed adjoint-fundamental matter, Phys. Rev. D **103**, 014503 (2021).

[35] N. Evans and K. S. Rigatos, Chiral symmetry breaking and confinement: separating the scales,, Phys. Rev. D **103**, 094022 (2021).

[36] A. Athenodorou, E. Bennett, G. Bergner, and B. Lucini, Infrared regime of SU(2) with one adjoint Dirac flavor, Phys. Rev. D **91**, 114508 (2015).

[37] Z. Bi, A. Grebe, G. Kanwar, P. Ledwith, D. Murphy, and M. L. Wagman, Lattice analysis of SU(2) with 1 adjoint Dirac flavor, *Proc. Sci.*, LATTICE2019 (2019) 127 [arXiv:1912.11723].

[38] A. Athenodorou, E. Bennett, G. Bergner, D. Elander, C. J. D. Lin, B. Lucini, and M. Piai, Large mass hierarchies from strongly-coupled dynamics, J. High Energy Phys. 06 (2016) 114.

[39] N. Seiberg and E. Witten, Electric-magnetic duality, monopole condensation, and confinement in $N = 2$ supersymmetric Yang-Mills theory, Nucl. Phys. **B426**, 19 (1994); N. Seiberg and E. Witten, Nucl. Phys. **B430**, 485 (E) (1994).

[40] C. Córdova and T. T. Dumitrescu, Candidate Phases for SU (2) Adjoint QCD4 with Two Flavors from N = 2 Supersymmetric Yang-Mills Theory, arXiv:1806.09592.

[41] L. Del Debbio, B. Lucini, A. Patella, and C. Pica, Quenched mesonic spectrum at large N, J. High Energy Phys. 03 (2008) 062.

[42] G. Bergner, I. Montvay, G. Münster, U. D. Özugurel, and D. Sandbrink, Towards The Spectrum of low-lying particles in supersymmetric Yang-Mills theory, J. High Energy Phys. 11 (2013) 061.

[43] B. Lucini, A. Rago, and E. Rinaldi, Glueball masses in the large N limit, J. High Energy Phys. 08 (2010) 119.

[44] A. Athenodorou, E. Bennett, G. Bergner, and B. Lucini, Investigating the conformal behaviour of SU(2) with one adjoint dirac flavor—data release, doi: https://doi.org/10.5281/zenodo.5139618 (2021).

[45] J. Giedt and E. Weinberg, Backward running or absence of running from Creutz ratios, Phys. Rev. D **84**, 074501 (2011).

[46] G. Cossu and M. D'Elia, Finite size phase transitions in QCD with adjoint fermions, J. High Energy Phys. 07 (2009) 048.

[47] G. Bergner and S. Piemonte, Compactified $N = 1$ supersymmetric Yang-Mills theory on the lattice: continuity and the disappearance of the deconfinement transition, J. High Energy Phys. 12 (2014) 133.

[48] G. Bergner, S. Piemonte, and M. Ünsal, Adiabatic continuity and confinement in supersym- metric Yang-Mills theory on the lattice, J. High Energy Phys. 11 (2018) 092.

[49] M. Lüscher, Properties and uses of the Wilson flow in lattice QCD, J. High Energy Phys. 08 (2010) 071; 03 (2014) 092 (E).

[50] E. Bennett and B. Lucini, Topology of minimal walking technicolor, Eur. Phys. J. C **73**, 2426 (2013).

[51] M. Luscher, Trivializing maps, the Wilson flow and the HMC algorithm, Commun. Math. Phys. **293**, 899 (2010).

[52] S. Borsanyi *et al.*, High-precision scale setting in lattice QCD, J. High Energy Phys. 09 (2012) 010.

[53] G. Bergner, P. Giudice, I. Montvay, G. Münster, and S. Piemonte, Influence of topology on the scale setting, Eur. Phys. J. Plus **130**, 229 (2015).

[54] V. Ayyar, T. DeGrand, M. Golterman, D. C. Hackett, W. I. Jay, E. T. Neil, Y. Shamir, and B. Svetitsky, Spectroscopy of SU(4) composite Higgs theory with two distinct fermion representations, Phys. Rev. D **97**, 074505 (2018).

[55] T. DeGrand and A. Hasenfratz, Remarks on lattice gauge theories with infrared-attractive fixed points, Phys. Rev. D **80**, 034506 (2009).

[56] T. DeGrand, Finite-size scaling tests for SU(3) lattice gauge theory with color sextet fermions, Phys. Rev. D **80**, 114507 (2009).

[57] B. Lucini, Strongly interacting dynamics beyond the Standard Model on a spacetime lattice, Phil. Trans. R. Soc. A **368**, 3657 (2010).

[58] L. Del Debbio and R. Zwicky, Hyperscaling relations in mass-deformed conformal gauge theories, Phys. Rev. D **82**, 014502 (2010).

[59] L. Del Debbio and R. Zwicky, Scaling relations for the entire spectrum in mass-deformed conformal gauge theories, Phys. Lett. B **700**, 217 (2011).

[60] S. M. Bhattacharjee and F. Seno, A measure of data collapse for scaling, J. Phys. A **34**, 6375 (2001).

[61] A. Patella, A precise determination of the psibar-psi anomalous dimension in conformal gauge theories, Phys. Rev. D **86**, 025006 (2012).

[62] A. Cheng, A. Hasenfratz, G. Petropoulos, and D. Schaich, Scale-dependent mass anomalous dimension from Dirac eigenmodes, J. High Energy Phys. 07 (2013) 061.

[63] A. Cheng, A. Hasenfratz, Y. Liu, G. Petropoulos, and D. Schaich, Finite size scaling of conformal theories in the presence of a near-marginal operator, Phys. Rev. D **90**, 014509 (2014).

[64] B. Lucini and M. Teper, SU(N) gauge theories in four-dimensions: Exploring the approach to $N = $ infinity, J. High Energy Phys. 06 (2001) 050.

[65] B. Lucini, M. Teper, and U. Wenger, Glueballs and k-strings in SU(N) gauge theories: Calculations with improved operators, J. High Energy Phys. 06 (2004) 012.

[66] A. G. Arroyo and C. K. Altes, The spectrum of Yang-Mills theory in a small twisted box, Nucl. Phys. **B311**, 433 (1988).

[67] D. Daniel, A. Gonzalez-Arroyo, C. K. Altes, and B. Soderberg, Energy spectrum of SU(2) Yang-Mills fields with space-like symmetric twist, Phys. Lett. B **221**, 136 (1989).

[68] D. Daniel, A. Gonzalez-Arroyo, and C. P. K. Altes, The Energy levels of lattice gauge theory in a small twisted box, Phys. Lett. B **251**, 559 (1990).